

Quantum limiting behaviors of a vortex core in an anisotropic gap superconductor

S. Kaneko, K. Matsuba, M. Hafiz, K. Yamasaki, E. Kakizaki, and N. Nishida
Department of Physics, Tokyo Institute of Technology, Tokyo 152-8551, Japan

H. Takeya and K. Hirata
National Institute for Materials Science, Tsukuba 305-0047, Japan

T. Kawakami, T. Mizushima, and K. Machida
Department of Physics, Okayama University, Okayama 700-8530, Japan
(Dated: June 3, 2019)

It is demonstrated both experimentally and theoretically that the quantized bound states at the vortex core are observed to be discretized in $\text{YNi}_2\text{B}_2\text{C}$. By using scanning tunneling spectroscopy with unprecedented 0.1nm spatial resolution, we find and identify the localized spectral structure where in addition to first the main peak with a positive low energy, the second sub-peak coming from the four-fold symmetric gap structure is seen inside the energy gap. Those spectral features are understood by solving the Bogoliubov-de Gennes equation for a full three dimensional gap structure. The spontaneous particle-hole symmetry breaking at the core site and the quantum oscillation in the spectra is clearly observed for the first time.

PACS numbers: 74.25.Uv, 74.25.Op

The quasiparticles (QP) bound in a vortex core, such as Majorana particle, are expected to play a fundamental role in various physical situations [1, 2], ranging from static and dynamical properties of vortex matter to quantum computation where it is required to exchange QPs bound in a core to encode a qubit through non-Abelian statistics[1, 3]. In order to isolate and manipulate those QPs, we need to identify those particles experimentally and theoretically as a first step. Namely we need to find the quantized energy levels for QPs spectroscopically, such as scanning tunneling microscopy and spectroscopy (STM/STS). This task is still on the way so far although several STM/STS experiments have probed the broad peak centered around the zero-bias energy $E = 0$ associated with the vortex bound states [4, 5], namely so-called Caroli-de Gennes-Matricon (CdGM) state [6], but those experiments can not resolve each discretized energy level fully quantum-mechanically. The origin of the difficulty in observing a discretized core bound state is due to (A) T should be low enough to satisfy the condition $T < T_c^2/\epsilon_F$ (T_c is the superconducting transition temperature and ϵ_F is the Fermi energy). (B) The spatial resolution of STM/STS should be fine enough to see the isolated bound state. Those two conditions have not been fulfilled in the exiting STM/STS experiments.

In our previous STS studies of the vortex bound state in $\text{YNi}_2\text{B}_2\text{C}$ at 0.46K [5], we have observed the broad peaks with electron-hole asymmetry in intensity in the tunneling spectrum around the center of the vortex core and interpreted them in terms of a quantum regime vortex core where the wave function of the hole-like bound state starts from zero at the center and that of the electron-like bound state does from maximum. In that experiment the spatial resolution was about 1nm and

the averaged spectra in the $2\text{nm} \times 2\text{nm}$ of the vortex core were measured. Here, we have performed STM/STS experiment at lower T (0.19K) with unprecedented spatial resolution ($\sim 0.1\text{nm}$), expecting to clarify a quantum nature of the vortex core states and a possible observation of new features such as quantum oscillations of QPs, on $\text{YNi}_2\text{B}_2\text{C}$ where $T_c=15.6\text{K}$, $H_{c2}=8.8\text{T}$, the mean free path $l=32\text{nm}$, the coherent length $\xi=6\text{nm}$ and the penetration depth $\lambda=110\text{nm}$. We also have theoretically analyzed to reveal the fact that the STS data indeed exhibit crucial information on the discretized quantum level structure.

A home-made scanning tunneling microscope is able to be operated at temperature down to 180mK and in magnetic fields up to 6T. We used Pt-Ir alloy wire with a diameter of 0.3mm that were mechanically sharpened in this experiment. Before cooling down the sample, we checked the tip condition over the Au film. STS measurements were conducted simultaneously with STM measurement. Using STM, we scan the sample for a wide surface where the square lattice can be seen. We choose a suitable spot and size range for the STS measurement. Bias voltage and feedback current are set before we start our measurement. We measured the I - V characteristic of the sample and calculated numerically differentiation of the I - V characteristic to find the differential conductance. We normalize the dI/dV with the slope value of the I - V characteristic by fitting it linearly. Then the vortex can be imaged by plotting the value of dI/dV at various biases.

In $\text{YNi}_2\text{B}_2\text{C}$ a variety of experiments [9–11] report on the existence of the point nodes, such as angle-resolved specific heat [9] and thermal conductivity [10]. From STS experiment, the tunneling spectrum was found to

have E^3 -dependence near $E = 0$ in the superconducting gap in zero magnetic field. In order to explain the E^3 -dependence, the existence of the point nodes with the asymmetric recovery and the need of 3D calculation were proposed [12]. Angle resolved photoemission measurement shows the strong gap magnitude variation on the cylindrical Fermi surface in the 17th bands at the X point of the tetragonal Brillouin zone of this material [11]. It is known that two dimensional d -wave nodal gap does not yield the isolated vortex bound state inside the bulk gap because all the low energy wave functions are extended, leaking out from the nodal directions [7], in contrast to the isotropic s -wave gap [8]. Thus it is not obvious for the point node case to exhibit the CdGM like bound state.

Our analytic tool is to solve the Bogoliubov-de Gennes (BdG) equation in three dimensions (3D) for various possible 3D gap functions, including the point node gap function on a cylindrical Fermi surface. The BdG formalism deals with the quantum limiting regime beyond the quasiclassical approximation [13–16] in the sense of the accessibility to discretized eigenstates and their quantum oscillation with the length scale of electrons.

In general, the BdG equation in spin singlet superconducting states is given as

$$\int d\mathbf{r}_2 \begin{bmatrix} H_0(\mathbf{r}_1, \mathbf{r}_2) & \Delta(\mathbf{r}_1, \mathbf{r}_2) \\ \Delta^*(\mathbf{r}_1, \mathbf{r}_2) & -H_0^*(\mathbf{r}_1, \mathbf{r}_2) \end{bmatrix} \vec{u}_\nu(\mathbf{r}_2) = E_\nu \vec{u}_\nu(\mathbf{r}_1), \quad (1)$$

where the single particle Hamiltonian $H_0 = \delta(\mathbf{r}_1 - \mathbf{r}_2) \left(-\frac{\hbar^2 \nabla^2}{2m} + V(\mathbf{r}_1) - \epsilon_F \right)$ and the QP wave function $\vec{u}_\nu(\mathbf{r}) = [u_\nu(\mathbf{r}), v_\nu(\mathbf{r})]^T$ with the Fermi energy ϵ_F . The pair potential $\Delta(\mathbf{r}_1, \mathbf{r}_2)$ is decomposed into $\Delta(\mathbf{R})$ in the center-of-mass coordinate $\mathbf{R} = (\boldsymbol{\rho}_1 + \boldsymbol{\rho}_2)/2$, where $\boldsymbol{\rho}_i = \mathbf{x}_i + \mathbf{y}_i$, and the gap function $\varphi(\tilde{\mathbf{r}})$ in the relative coordinate $\tilde{\mathbf{r}} = \mathbf{r}_1 - \mathbf{r}_2$. Here, we consider the single vortex state described as $\Delta(\mathbf{R}) = \Delta_0 \tanh(|\mathbf{R}|/\xi) \exp(i\phi)$, where the coherence length $\xi = \epsilon_F / (2\Delta_0 k_F)$ and the azimuthal angle $\phi = \arctan[(x_1 + x_2)/(y_1 + y_2)]$. In this model, the wave number k_z becomes a well-defined quantum number because of the translation symmetry along the z axis. The BdG equation (1) is reduced to the k_z -resolved two-dimensional form:

$$\int d\boldsymbol{\rho}_2 \begin{bmatrix} H_0(\boldsymbol{\rho}_1, \boldsymbol{\rho}_2) & \Delta(\mathbf{R})\varphi_{k_z}(\tilde{\boldsymbol{\rho}}) \\ \Delta^*(\mathbf{R})\varphi_{k_z}(\tilde{\boldsymbol{\rho}}) & -H_0^*(\boldsymbol{\rho}_1, \boldsymbol{\rho}_2) \end{bmatrix} \vec{u}_{\nu, k_z}(\boldsymbol{\rho}_2) = E_{\nu, k_z} \vec{u}_{\nu, k_z}(\boldsymbol{\rho}_1), \quad (2)$$

where $H_0 = \delta(\boldsymbol{\rho}_1 - \boldsymbol{\rho}_2) \left(-\frac{\hbar^2 \nabla'^2}{2m} + V(\boldsymbol{\rho}_1) - \epsilon_F^{2D}(k_z) \right)$ and $\nabla'^2 = \partial_x^2 + \partial_y^2$. The two-dimensional form of the Fermi energy $\epsilon_F^{2D}(k_z) = \frac{\hbar^2}{2m}(k_F^2 - k_z^2)$ reflects the k_z -cross section of the Fermi surface. The index $\nu \in \mathbb{Z}$ denotes the ν -th excited state of the k_z -resolved BdG equation (2). The gap function $\varphi_{k_z}(\boldsymbol{\rho}) = \frac{1}{(2\pi)^2} \int dk_x dk_y \varphi_{\mathbf{k}} e^{i\mathbf{k} \cdot \boldsymbol{\rho}}$ is obtained from $\varphi_{\mathbf{k}}$ in the \mathbf{k} -space by performing the fast Fourier

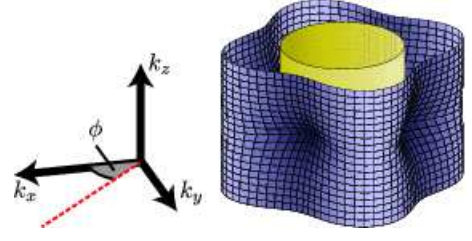


FIG. 1: (Color online) schematic view of the gap function and definition of the angle ϕ drawn on the cylindrical Fermi surface used in the calculation.

transform. We can solve the BdG equation for the arbitrary anisotropic function $\varphi_{\mathbf{k}}$. Then, we obtain the QP local density of states (LDOS):

$$\mathcal{N}(\boldsymbol{\rho}, E) = \sum_{k_z} \mathcal{N}_{k_z}(\boldsymbol{\rho}, E) = \sum_{\nu, k_z} |u_{\nu, k_z}(\boldsymbol{\rho})|^2 \delta_\eta(E - E_{\nu, k_z}),$$

with the Lorentzian function $\delta_\eta(z) = \eta^2 / [z^2 + \eta^2]$. The value η is adjusted to compare the experimental data of the STS measurements below.

Within the BCS theory, $\varphi_{\mathbf{k}}$ is non-zero near the Fermi surface. Therefore, we employ the model described as $\varphi_{\mathbf{k}} = \varphi_{\hat{\mathbf{k}}} \exp[-(k - k_F)^2 \xi_p]$, where ξ_p is the size of the Cooper pair, where $\xi_p \sim k_F^{-1}$. The function $\varphi_{\hat{\mathbf{k}}}$ represents the anisotropy of the pairing function in the relative momentum space \mathbf{k} . When the function $\varphi_{\hat{\mathbf{k}}}$ is smooth in the k_x - k_y space, $\varphi_{k_z}(\boldsymbol{\rho})$ is localized within the range $|\tilde{\boldsymbol{\rho}}| \lesssim k_F^{-1}$ which decreases exponentially on $|\tilde{\boldsymbol{\rho}}|$. The localization of the gap function within $|\tilde{\boldsymbol{\rho}}| \lesssim k_F^{-1}$ confines $\Delta(\mathbf{r}_1, \mathbf{r}_2)$ to a band matrix. The resulting BdG equation (2) is solved numerically by using the finite element method implemented with the discrete variable representation (FEMDVR) [17–19]. This allows us to solve the two-dimensional eigenvalue problem with 200×200 FEMDVR grids (corresponding to the system size $200k_F^{-1}$) within the 32 GB main memory. The diagonalization of a huge matrix is performed with the shift-invert Lanczos algorithm [20].

It is considered that the gap function of the $\text{YNi}_2\text{B}_2\text{C}$ is suppressed at four points, where nesting vectors exist [15, 21]. We parametrize the gap function as

$$\varphi_{\hat{\mathbf{k}}} = \frac{1}{2} \{1 + \varphi_{\min}(k_z) + [1 - \varphi_{\min}(k_z)] \cos 4\phi_k\} \quad (3)$$

where the angle $\phi_k = \arctan(k_x/k_y)$ and in-plane gap minimum $\varphi_{\min}(k_z) = \varphi_0 [\tanh(k_z/\alpha k_1)]^n$. This gap function is equivalent to the $s+g$ -wave gap [21] function in the $k_z = 0$ plane and parameters α , n , φ_0 signify how quickly the point nodes at the $k_x = 0$ and $k_y = 0$ plane recover the full gap with increasing k_z toward the Brillouin zone boundary at $k_z = k_1$. We choose the cylindrical Fermi surface as the first approximation, where $\epsilon_F^{2D}(k_z)$ is constant. This is because we focus on the 17th Fermi surface around X point of $\text{YNi}_2\text{B}_2\text{C}$, which does not close

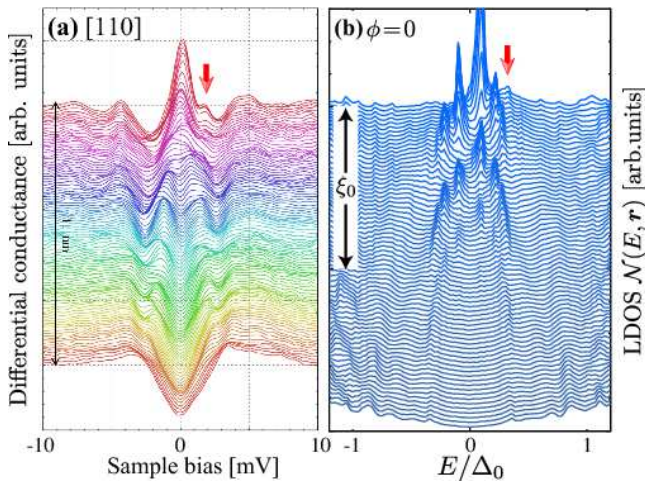


FIG. 2: (Color online) (a) The differential conductance at $T=190\text{mK}$ and $H=0.3\text{T}$ as a function of the sample bias obtained by STS measurements for [110] direction. The spacing between each spectrum is 0.11nm . The total path length is 11nm . (b) The spectral evolutions of the LDOS $D(E, \mathbf{r})$ for anti-nodal direction. The spatial scale is denoted by the long arrows with the length ξ_0 . The short down arrows in the back indicate the shoulder structure at the core. It is seen that several low energy peaks near $E = 0$ oscillate and evolve in their intensities as a function of the position from the core.

in the Brillouin zone as obtained by the band calculation [22]. Figure 1 shows a three dimensional view of $\varphi_{\hat{\mathbf{k}}}$ along with the cylindrical Fermi surface. As we will see later, the combination of the Fermi surface shape and the gap function along the k_z direction is crucial to reproduce the STS data. We carry out the calculation within the quantum limit regime $k_F \xi = 10$. In the case of the $\text{YNi}_2\text{B}_2\text{C}$, the direction of the Fermi velocity \mathbf{v}_F at the gap nodes [22] is different by $\pi/4$ from that of the wave vector \mathbf{k}_F , so that the low-energy QP spectrum is rotate by $\pi/4$ from the isotropic case $\mathbf{v}_F \parallel \mathbf{k}_F$ [16]. Thus, the spectrum along the [110] ([100]) axis in our experiments corresponds to that along the $\phi = 0$ ($\pi/4$) in our calculations.

Figure 2 shows the experimental (a) and theoretical (b) spectral evolution along a direction (a) [110] and (b) $\phi = 0$. In the experimental data shown in Fig. 2(a), it is evident to see that (i) the main peak at the core site shifts to the positive energy side. (ii) The 2nd peak at the core site exists at the positive bias $E \sim 1.5 \text{ meV}$, marked with the arrow in Fig. 2(a). (iii) The spatial modulated behavior appears on the evolution ridge. We note that the average of the present STS data with 0.1nm spatial resolution in $2\text{nm} \times 2\text{nm}$ well reproduce the previous STS results of tunneling spectra by Nishimori *et al.* [5]. These features (i)-(iii) are supported by the numerical calculation shown in Fig. 2(b). In particular, in Fig. 2(b), the feature (iii) is interpreted as the quantum oscillations of the peak intensities associated with several lower energy

excitations. We also find that (iv) quantum oscillation depends on either $\phi = 0$ or $\pi/4$ directions. The finite energy spectrum near $E/\Delta_0 \sim 0.3$ in the $\phi = 0$ direction extend longer than that in the $\phi = \pi/4$ direction. This angular dependence is also shown in the experimental data as the difference between the evolution of the [110] and [100] direction. These consistencies with the theory denote that the experimental data in Fig. 2 observes the quantum limiting behaviors of the vortex core bound states whose discreteness is specified by the energy scale $\Delta_0^2/\epsilon_F^{2D}$. It is also found that the spherical or ellipsoidal Fermi surface smoothes the quantum oscillation of the LDOS. Hence, the cylindrical Fermi surface is necessary for the quantum oscillation.

It is emphasized that the 2nd peak which appears at $E/\Delta_0 \sim 0.3$ seen in Fig. 2 is a consequence of the rotational symmetry due to the point nodes and never seen in the LDOS of isotropic s -wave superconductors [8]. In order to understand the physical origin of the 2nd peak, we decompose the spectrum into the k_z -resolved spectra as shown in Fig. 3(a) where the k_z -resolved spectra at the core are displayed. The strong peak at $E/\Delta_0 = 0.1$ is associated with the lowest bound state $\nu = 1$. This $\nu = 1$ peak becomes stronger and shifts to the positive side as k_z increases because the gap becomes wider. Simultaneously the 2nd peak at $E/\Delta_0 = 0.3$ grows and is distinctly separated from the main $\nu = 1$ peak when $k_z \neq 0$. Figure 3(b) shows the k_z -resolved eigenenergy of the BdG equation (2). At $k_z = 0$, where the in-plane gap minimum has $\varphi_{\min}(k_z = 0) = 0$, the spectrum is continuous, and the eigenstates with E/Δ_0 lower than the gap minimum φ_{\min} become discrete with increasing φ_{\min} . The $\nu = 5$ eigenenergy is marked in Fig. 3 with the filled symbols, which consists of the 2nd peak in the LDOS.

The physical origin is explained as follows. As $\varphi_{\min} \rightarrow 1$, where the limit of an two-dimensional isotropic s -wave case [8], the branches of the eigenstates ν approach to the eigenstates quantized by the angular momentum $\ell = 1/2, 3/2, 5/2, \dots$ with the energy $E_{\ell+1/2, k_z} = \ell\omega_0$, where $\omega_0 \sim \Delta_0^2/2\epsilon_F^{2D}$, and the wave function $u_{\ell+1/2, k_z}(\boldsymbol{\rho}) \propto J_{\ell-1/2}(k_F \rho)$ near the vortex core, where $J_\nu(x)$ is the Bessel function [6, 8]. The only $\ell = 1/2$ state has the nonzero core-site wave function $u_{\ell+1/2, k_z}(\boldsymbol{\rho} = 0) \neq 0$. When $\varphi_{\min} < 1$, however, the four-fold rotationally symmetric pair potential hybridizes the eigenstates with the angular momentum $\ell + 4n$ ($n \in \mathbb{Z}$) [13]. Thus, the $\ell = 1/2$ state can be hybridized to the $\ell = 1/2 + 4n$ states, which are realized as the $\nu = 4n + 1$ states described as

$$u_{4n+1}(\boldsymbol{\rho}) = \sum_{n'} a_n^{n'} J_{4n'}(k_F \rho) e^{-i4n\phi}, \quad (4)$$

This $n' = 0$ contribution originating from the $\ell = 1/2$ state in the wave function $u_{\nu=5}$ gives origin to the 2nd peak of the core-site LDOS. The peak arising from the $\nu = 5$ state is the most enhanced because the $\ell = 9/2$

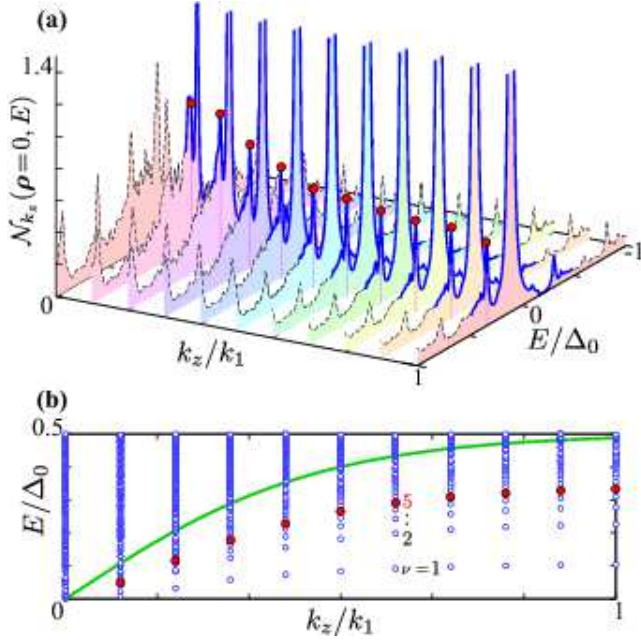


FIG. 3: (Color online) (a) The k_z -resolved spectra $\mathcal{N}_{k_z}(r=0, E)$ at the core. The solid (broken) line indicates inside (outside) of the in-plane gap minimum $\Delta_0\varphi_{\min}$. It is seen that as k_z increases the 2nd peak structure at $E/\Delta_0 = 0.3$ becomes split from the main peak at $E = 0.1$. (b) The k_z -resolved eigenenergy E_{ν, k_z} (symbols) and the gap minimum $\Delta_0\varphi_{\min}$ (line). Filled symbols in the both panels denote the eigenenergy $E_{\nu=5, k_z}$, the 5th excited state of the k_z resolved BdG equation (2).

state is the nearest energy state from the $\ell = 1/2$ state. Although there exist the peaks from the $\nu = -3, 9 \dots$ states in the k_z -resolved core-site LDOS, these peaks cannot be seen in Fig. 2(b) as well as (a) with the k_z integration.

Next, we move to the two-dimensional profile of the LDOS. Figure 4 shows that the experimental and theoretical two-dimensional LDOS with different energies. It is known that the LDOS has the long tail along the nodal direction $\phi = \pi/4$ near $E=0$, and as the energy increases the direction of the tails rotates to the $\phi = 0$ in the case of the four-fold rotationally symmetric gap function at low energy. The recent improvement on the space and energy resolution of the STS measurements allows us to observe the spatial modulation of the LDOS with the length scale of electrons shown in Fig. 4(a) and (b). We obtain the two-dimensional quantum oscillation theoretically, and find that the direction of the oscillations also rotates by $\pi/4$ with growth of the energy. These oscillatory behaviors are understandable with the schematic picture of the QP path shown in Fig. 4(e). In the four-fold rotationally symmetric gap function, the low energy QPs move from $\phi = \pi/4$ direction to the $\phi = -\pi/4$ direction around the vortex core [13–16]. The interference between the wave functions of the countercurrent QPs

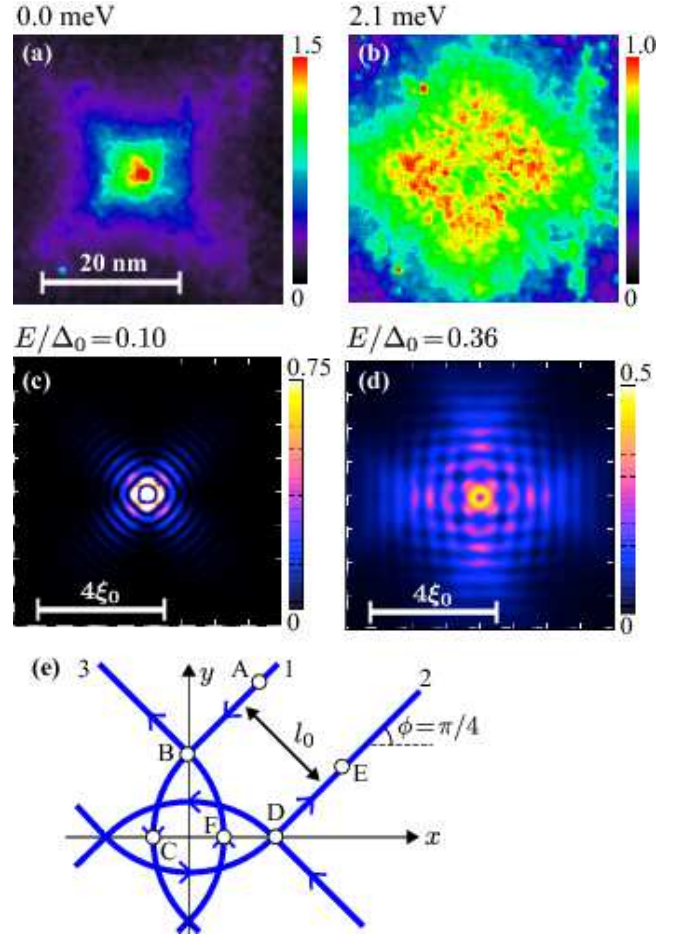


FIG. 4: (Color online) The experimental differential conductance dI/dV with the sample biases $E = 0.0$ meV (a) and $E = 2.1$ meV (b) at $T=180$ mK and $H=0.3$ T. The corresponding two-dimensional LDOS map $\mathcal{N}(E=0.1\Delta_0, \rho)$ (c) and $\mathcal{N}(E=0.36\Delta_0, \rho)$ (d). The panel (e) shows the schematic figure of the QP paths with the large contribution when the vortex core exists at the origin.

leads to the standing wave, that is, the oscillation of the LDOS. When the energy is $E \sim 0$ and the distance is $l_0 \ll k_F^{-1}$ in Fig. 4(e), the QP “1” moving from A to B and “2” moving from D to E interfere with each other. The resulting wave front direction of the standing wave is $\phi = \pm\pi/4$ as shown in Fig. 4(c). On the other hand, when the energy E becomes large, the distance between paths becomes large as $l_0 \gtrsim k_F^{-1}$ with the growth of the impact parameter. The large l_0 allows to form the interference pattern by the QP “1” moving from B to C and “3” moving from F to B in Fig. 4(e). Thus, the LDOS oscillation pattern appears along the $\phi = 0, \pi/2$ direction in the high energy region $E/\Delta_0 = 0.36$ as shown in Fig. 4(d). The change of the orientation of the LDOS is clearly observed in experiments as in Fig. 4. To observe the rotation of the oscillation pattern remains a future problem.

We have performed STM/STS experiments on $\text{YNi}_2\text{B}_2\text{C}$ under the unprecedented spatial resolution with $\sim 0.1\text{nm}$ at low temperatures. Through the full quantum mechanical analysis based on the Bogoliubov-de Gennes equation for three dimensional gap structure, we have succeeded in identifying at the core position the quantized bound state at a positive energy as the first peak, resulting in the spontaneous particle-hole symmetry breaking. We have also found the second peak induced by the four-fold symmetric gap structure. This is the first experimental observation of the Caroli-de Gennes-Matricon vortex bound states that are clearly discretized. We conclude that in reciprocal space the point node positions correspond to the continuum spectra with the zero energy while the gapped positions give rise to the discrete spectra.

We are grateful to M. Ichioka for stimulating discussion. This work was supported in part by a 21st Century G-COE Program at Tokyo tech "Nano Science and Quantum Physics", JSPS, and the "Topological Quantum Phenomena" KAKENHI on innovation areas from MEXT.

-
- [1] C. Nayak, S. H. Simon, A. Stern, M. Freedman, and S. Das Sarma, *Rev. Mod. Phys.* **80**, 1083 (2008).
- [2] M. Z. Hasan and C. L. Kane, *Rev. Mod. Phys.* **82**, 2045 (2010).
- [3] D. A. Ivanov, *Phys. Rev. Lett.* **86**, 268 (2001).
- [4] H. F. Hess, R. B. Robinson, R. C. Dynes, J. M. Valles, and J. V. Waszczak, *Phys. Rev. Lett.* **62**, 214 (1989).
- [5] H. Nishimori, K. Uchiyama, S. Kaneko, A. Tokura, H. Takeya, K. Hirata, and N. Nishida, *J. Phys. Soc. Jpn.* **73**, 3247 (2004).
- [6] C. Caroli, P. G. de Gennes, and J. Matricon, *Phys. Lett.* **9**, 307 (1964).
- [7] M. Franz and Z. Tešanović, *Phys. Rev. Lett.* **80**, 4763 (1998).
- [8] N. Hayashi, T. Isoshima, M. Ichioka, and K. Machida, *Phys. Rev. Lett.* **80**, 2921 (1998).
- [9] T. Park, M. B. Salamon, E. M. Choi, H. J. Kim, and S. I. Lee, *Phys. Rev. Lett.* **90**, 177001 (2003).
- [10] K. Izawa, K. Kamata, Y. Nakajima, Y. Matsuda, T. Watanabe, M. Nohara, H. Takagi, P. Thalmeier, and K. Maki, *Phys. Rev. Lett.* **89**, 137006 (2002).
- [11] T. Baba, T. Yokoya, S. Tsuda, T. Watanabe, M. Nohara, H. Takagi, T. Oguchi, and S. Shin, *Phys. Rev. B* **81** 180509(R) (2010).
- [12] H. Nishimori, Doctor Thesis (Tokyo Institute of Technology, 2005) in Japanese.
- [13] M. Ichioka, N. Hayashi, N. Enomoto, and K. Machida, *Phys. Rev. B* **53** 15316 (1996).
- [14] N. Hayashi, M. Ichioka, and K. Machida, *Phys. Rev. Lett.* **77**, 4074 (1996).
- [15] Y. Nagai, Y. Ueno, Y. Kato, and N. Hayashi, *J. Phys. Soc. Jpn.* **75** 104701 (2006).
- [16] Y. Nagai, Y. Kato, N. Hayashi, K. Yamauchi, and H. Harima, *Phys. Rev. B* **76** 214514 (2007).
- [17] J. C. Light, I. P. Hamilton, and J. V. Lill, *J. Chem. Phys.* **82**, 1400 (1985).
- [18] T. N. Rescigno and C. W. McCurdy, *Phys. Rev. A* **62**, 032706 (2000).
- [19] T. Mizushima and K. Machida, *Phys. Rev. A* **82**, 023624 (2010); *J. Low Temp. Phys.* **162**, 204 (2011).
- [20] The subroutine libraries are available from the home page at [<http://www.caam.rice.edu/software/ARPACK>].
- [21] K. Maki, P. Thalmeier, and H. Won, *Phys. Rev. B* **65**, 140502(R) (2002).
- [22] K. Yamauchi, H. Katayama-Yoshida, A. Yanase, and H. Harima, *Physica C* **412-414**, 225 (2004).